VOL. 54, NO. 24 JOURNAL OF THE ATMOSPHERIC SCIENCES 15 DECEMBER 1997

Parameterizing Grid-Averaged Longwave Fluxes for Inhomogeneous Marine Boundary Layer Clouds

HOWARD W. BARKER

Cloud Physics Research Division, Atmospheric Environment Service, Downsview, Ontario, Canada

BRUCE A. WIELICKI

Atmospheric Sciences Division, NASA/Langley Research Center, Hampton, Virginia

(Manuscript received 6 November 1996, in final form 6 May 1997)

ABSTRACT

This paper examines the relative impacts on grid-averaged longwave flux transmittance (emittance) for marine boundary layer (MBL) cloud fields arising from horizontal variability of optical depth τ and cloud sides. First, using fields of Landsat-inferred τ and a Monte Carlo photon transport algorithm, it is demonstrated that mean all-sky transmittances for 3D variable MBL clouds can be computed accurately by the conventional method of linearly weighting clear and cloudy transmittances by their respective sky fractions. Then, the approximations of decoupling cloud and radiative properties and assuming independent columns are shown to be adequate for computation of mean flux transmittance.

Since real clouds have nonzero geometric thicknesses, cloud fractions $\hat{A}_c$ presented to isotropic beams usually exceed the more familiar vertically projected cloud fractions A_c. It is shown, however, that when $A_c \lesssim 0.9$, biases for all-sky transmittance stemming from use of A_c as opposed to $\hat{A}_c$ are roughly 2–5 times *smaller* than, and opposite in sign to, biases due to neglect of horizontal variability of τ. By neglecting variable τ, all-sky transmittances are underestimated often by more than 0.1 for A_c near 0.75 and this translates into relative errors that can exceed 40% (corresponding errors for all-sky emittance are about 20% for most values of A_c). Thus, priority should be given to development of general circulation model (GCM) parameterizations that account for the effects of horizontal variations in unresolved τ; effects of cloud sides are of secondary importance.

On this note, an efficient stochastic model for computing grid-averaged cloudy-sky flux transmittances is furnished that assumes that distributions of τ, for regions comparable in size to GCM grid cells, can be described adequately by gamma distribution functions. While the plane-parallel, homogeneous model underestimates cloud transmittance by about an order of magnitude when 3D variable cloud transmittances are $\lesssim 0.2$ and by ~20% to 100% otherwise, the stochastic model reduces these biases often by more than 80%.

1. Introduction

While there is a wealth of studies aimed at shortwave radiative transfer for inhomogenous clouds (Welch and Wielicki 1984; Davis et al. 1990; Barker 1992; Cahalan et al. 1994a), there is a dearth of studies regarding the impact of inhomogeneities on longwave (LW) radiative transfer (e.g., Harahvardhan et al. 1981; Ellingson 1982; Evans 1993). In remote sensing and climate modeling studies, clouds are usually assumed to be horizontally homogeneous and occasionally assumed to be black in the LW portion of the spectrum. For (60 km)^2 regions of marine boundary layer (MBL) clouds, however, Barker et al. (1996) showed that small values of cloud optical depth τ are often very abundant even when mean τ is much larger than 0 (see also Wielicki and Parker 1992, 1994). Thus, since LW radiative transfer is an extremely nonlinear process for small τ, it is reasonable to expect that grid-averaged LW transmittances and emissivities, as required by general circulation models (GCMs), may be sensitive to unresolved horizontal inhomogeneities of cloud.

A case in point supporting this expectation is Wielicki and Parker's (1992) assertion that by neglecting translucent clouds, the spatial coherence method (Coakley and Bretherton 1982) often underestimates MBL cloud fraction by 0.15–0.2. Heeding this, Luo et al. (1994) extended the spatial coherence method and deduced that for (250 km)^2 regions of marine stratocumulus clouds off the coast of South America, grid-averaged 11-μm emissivities for *clouds only* are often closer to the value of cloud fraction than to unity. For this to be true, not only must there often be substantial amounts of thin cloud amid readily observable thicker cloud, but the inhomogeneous nature of these clouds is likely impor-

Corresponding author address: Howard Barker, Atmospheric Environment Service, Cloud Physics Research Division (ARMP), 4905 Dufferin St., Downsview, ON M3H 5T4, Canada.
E-mail: howard.barker@ec.gc.ca

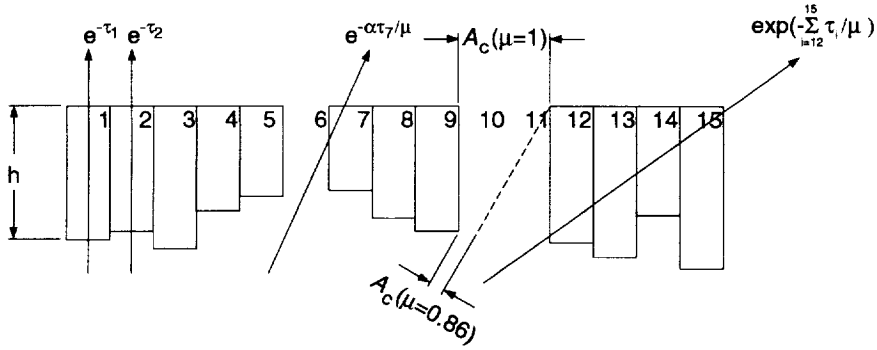

FIG. 1. Schematic 2D cross section of a cloud field (consisting of 15 cells) with geometric thicknesses h_i and vertically projected cloud fraction 0.8. For lines-of-sight 30° from the zenith ($\mu \approx 0.86$), however, apparent cloud fraction is almost 100%. Note that distributions of optical depth encountered by zenith traveling radiances (e.g., those depicted on the left) are composed of τ_i only, whereas those for off-zenith radiances (e.g., the one grazing cell 7) consist, in part, of $\alpha\tau_i$ where $\alpha \leq 1$. Also for off-zenith radiances, distributions of optical depth consist of spatially averaged values such as that associated with the radiance spanning cells 12 through 15.

tant for LW radiative transfer and thus cloud heating rates.

In addition to unresolved fluctuations in τ, numerous studies have demonstrated the importance of cloud sides in radiative transfer for broken clouds fields (e.g., Harshvardhan et al. 1981; Ellingson 1982; Zuev and Titov 1995). Yet for LW radiative transfer, the relative impacts of cloud sides and horizontal fluctuations in τ have not been delineated.

The main purpose of this paper is to examine the impacts on grid-averaged LW transmittance (emittance) for inhomogeneous MBL clouds arising from cloud fluctuations at scales unresolved by GCMs. Section 2 gives a background discussion of LW flux transmittance for inhomogeneous MBL clouds. In section 3, optical depths inferred from Landsat data are presented briefly. These data are used in section 4 as input for a Monte Carlo photon transport algorithm, the results of which culminate in an assessment of the relative impact of cloud sides and horizontal variability of τ. Section 5 presents an approximate technique for computing grid-averaged cloudy-sky transmittance that assumes that τ are distributed according to the gamma distribution function and that the independent pixel approximation (see Cahalan et al. 1994a,b; Barker 1996) applies for LW radiation. Concluding remarks are in section 6.

2. Longwave transmittance for horizontally inhomogeneous cloud: A conceptual model

To begin, assume that the intensity of a pencil of LW radiation is extinguished by clouds in accordance with the Beer–Bouger–Lambert law and that multiple scattering by droplets can be neglected since droplet single scattering albedo ω_0 is small (<0.5) and asymmetry parameter g is large (>0.9) for much of the atmospheric window. Thus, throughout this study, τ symbolizes LW absorption optical depth, which equals $(1 - \omega_0)\tau_{ext}$ where τ_{ext} is extinction optical depth. Furthermore, extinction by gases is neglected in order to simplify the presentation and since only boundary layer clouds are considered; all clouds are assumed to be isothermal.

Figure 1 shows a schematic diagram of the main concerns involving LW radiative transfer through horizontally inhomogeneous boundary layer clouds. Consider viewing this cloud (field) at different zenith angles, θ ($\mu = \cos\theta$). For simplicity, all quantities throughout this study are assumed to be azimuthal averages. The probability of a line-of-sight being intercepted by cloud is a function of μ, minimized for $\mu = 1$ and increasing monotonically as μ decreases. This probability can be thought of as the zenith-angle-dependent cloud fraction $A_c(\mu)$. The form of $A_c(\mu)$ depends on several factors including distributions of cloud size (Wielicki and Welch 1986), aspect ratio (Plank 1969), and spacing (Cahalan 1991). For nonovercast clouds, the strongest and weakest dependencies of $A_c(\mu)$ on μ are probably associated with fields of towering clouds and MBL clouds, respectively. Given that observations and radiative fluxes are affected by $A_c(\mu)$, when cloud fractions are reported for observations and GCMs, it is unclear what is being, and what should be, discussed. It seems likely that the most common interpretation of the term *cloud fraction* is the vertically projected value $A_c(1)$. This quantity, however, is likely neither that reported in cloud atlases nor that most meaningful for computation of radiative fluxes in GCMs (i.e., 1D column models).

Next, consider probability distributions of cloud optical depth τ (normalized to the vertical as usual) for lines of sight along given zenith angles. Denote these distributions of τ conditional upon μ as $p(\tau|\mu)$. As can be inferred from the idealized clouds in Fig. 1, one can expect $p(\tau|1)$ to be relatively broad but as $\mu \to 0$, $p(\tau|\mu)$ will tend to become narrower and more symmetric about the zenith-angle-dependent mean cloud optical depth $\bar{\tau}(\mu)$. This is because averaging optical depth

along oblique lines through a cloud field is a form of horizontal smoothing that is somewhat analogous to the narrowing of $p(\tau|1)$ as the resolution of a cloud field degrades (e.g., Schertzer and Lovejoy 1987). Likewise, the form of $\overline{\tau}(\mu)$ will depend on the geometry of the cloud field. For example, the clouds in Fig. 1 have thin wedges near their tops and sides that are exposed to lines of sight with $\mu < 1$. Thus, one would expect $\overline{\tau}(\mu)$, and the variance of τ, to decrease slightly with decreasing μ.

Taking the cloudless and cloudy parts of a region together, the grid-averaged, all-sky distribution of optical depth conditional upon μ is

$$\mathcal{P}(\tau|\mu) = [1 - A_c(\mu)]\delta(\tau) + A_c(\mu)p(\tau|\mu), \quad (1)$$

where $\delta(\tau)$ is the integrand of the Dirac function. Assuming that

$$\int_0^\infty p(\tau|\mu)\,d\tau = 1 \quad \text{and} \quad \int_0^\infty \tau p(\tau|\mu)\,d\tau = \overline{\tau}(\mu), \quad (2a)$$

$\mathcal{P}(\tau|\mu)$ is also normalized as

$$\int_0^\infty \mathcal{P}(\tau|\mu)\,d\tau = 1 - A_c(\mu) + A_c(\mu) = 1, \quad (2b)$$

with grid-averaged zenith-angle-dependent optical depth of

$$\int_0^\infty \tau\mathcal{P}(\tau|\mu)\,d\tau = 0 + A_c(\mu)\int_0^\infty \tau p(\tau|\mu)\,d\tau = A_c(\mu)\overline{\tau}(\mu). \quad (2c)$$

Similar expressions exist, of course, for all moments of $\mathcal{P}(\tau|\mu)$.

Letting radiance transmittances through cloud and clear air be $e^{-\tau/\mu}$ and 1, respectively, grid-averaged all-sky transmittance T for an isotropic distribution of incident radiation is

$$T = 2\int_0^\infty\int_0^1 \{[1 - A_c(\mu)]\delta(\tau) + A_c(\mu)p(\tau|\mu)e^{-\tau/\mu}\}\mu\,d\mu\,d\tau$$
$$= 1 - \hat{A}_c + \underbrace{2\int_0^\infty\int_0^1 A_c(\mu)p(\tau|\mu)e^{-\tau/\mu}\mu\,d\mu\,d\tau}_{\text{cloudy-sky contribution}}, \quad (3)$$

in which

$$\hat{A}_c = 2\int_0^1 A_c(\mu)\mu\,d\mu \quad (4)$$

could be referred to as the *hemispherical cloud fraction.* Like $A_c(1)$, $\hat{A}_c$ is almost certainly neither cloud fraction estimated by, and used in, GCMs nor cloud fraction reported in cloud atlases. Moreover, the cloudy-sky contribution in (3) shows that, in principle, radiation fields and cloud fraction cannot be decoupled in a straightforward manner, even when scattering is ignored. Stephens (1988) discussed this issue and showed that for LW radiative transfer through opaque clouds, T can be expressed as a linear combination of clear and cloudy transmittances weighted by suitable clear and cloudy fractions. This approximation is ubiquitous to climate studies and, when applied to (3), it becomes

$$T = 1 - \hat{A}_c + \hat{A}_c T_{\text{cld}}, \quad (5a)$$

where

$$T_{\text{cld}} = 2\int_0^\infty\int_0^1 p(\tau|\mu)e^{-\tau/\mu}\mu\,d\mu\,d\tau = 1 - \varepsilon_{\text{cld}} \quad (5b)$$

is grid-averaged cloud transmittance and ε_{cld} is corresponding emissivity.

For a plane-parallel, homogeneous (PPH) cloud of optical depth $\overline{\tau}$, $p(\tau|\mu) = \delta(\tau - \overline{\tau})$, which, when substituted into (5b), gives the familiar result

$$T_{\text{cld}}^{\text{PP}} \equiv 2\int_0^1 e^{-\overline{\tau}/\mu}\mu\,d\mu = 2E_3(\overline{\tau}) = 1 - \varepsilon_{\text{cld}}^{\text{PP}}, \quad (6)$$

where $E_3(\overline{\tau})$ is the third-order exponential integral (Charlock and Herman 1976). Often, $T_{\text{cld}}^{\text{PP}}$ is expressed as $e^{-\mathcal{D}\overline{\tau}}$, where $\mathcal{D}$ is the diffusivity factor (Elsasser 1942; Stephens 1978). Quanhua and Schmetz (1987) expressed $\mathcal{D}$ as a function of $\overline{\tau}$ such that $e^{-\mathcal{D}\overline{\tau}}$ is equivalent to (6). Wielicki and Parker (1994) and Barker et al. (1996) showed, however, that for MBL clouds, it is often the case that large fractions of area have small τ, even for $\overline{\tau} \gg 0$. Thus, at times, it can be expected that the nonlinear effects of averaging $e^{-\tau/\mu}$ or $E_3(\tau)$ over all τ will yield results that differ greatly from $T_{\text{cld}}^{\text{PP}}(\overline{\tau})$. Given that cloud fractions reported in cloud climatologies include thin clouds (Rossow and Schiffer 1991), and that future climatologies will report even thinner clouds (see Wylie et al. 1994), GCMs will have to account for these thin clouds in order to make validation of simultaneously predicted cloud fraction and radiative budgets as unambiguous as possible. It stands to reason, therefore, that the radiative impact of *all* clouds should also be addressed by GCMs. Hence, it may be essential, at times, to utilize forms of T_{cld} and $\hat{A}_c$ that are less trivial than $T_{\text{cld}}^{\text{PP}}$ and $A_c(1)$.

Thus, the primary objectives of this study, in the context of MBL clouds only, may now be stated clearly as (i) to establish the applicability of (5a), (ii) to deduce the necessity for parameterizing $\hat{A}_c$, and (iii) to establish a suitable parameterization for T_{cld}. Investigations are conducted using fields of Landsat-inferred cloud optical depths as input to a Monte Carlo photon transport algorithm.

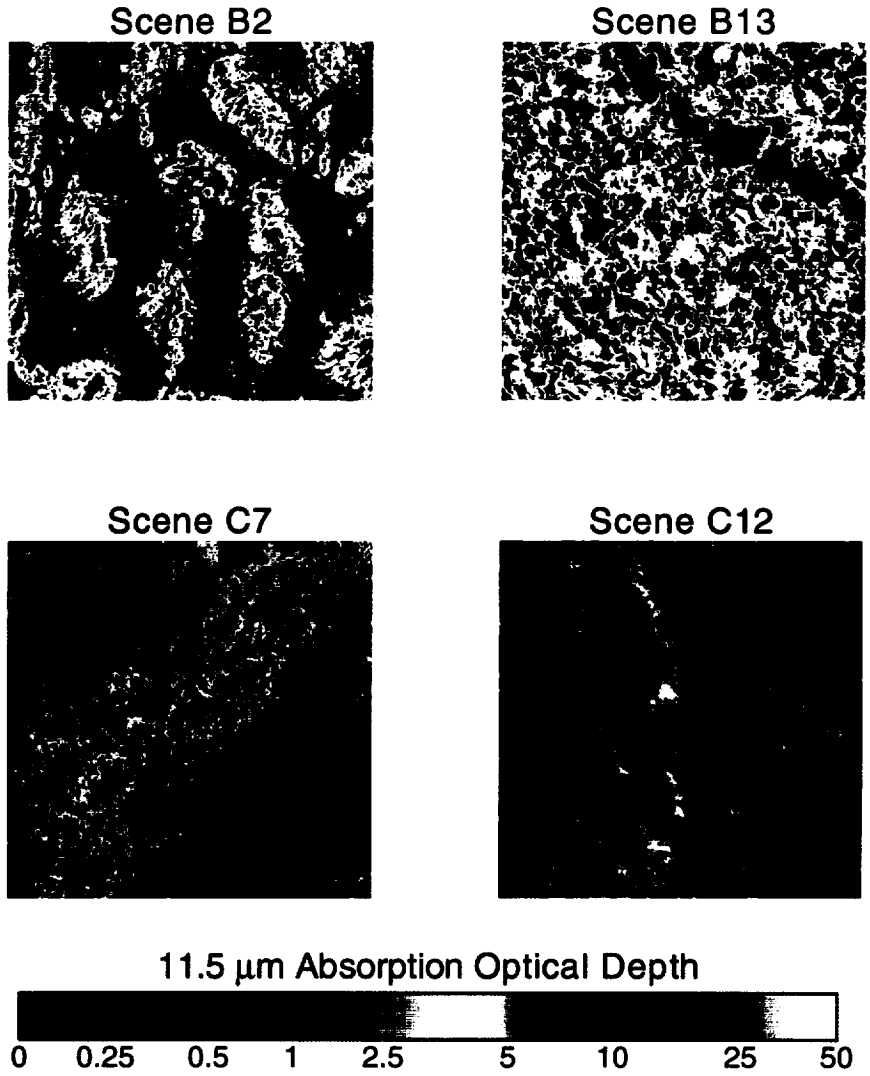

FIG. 2. Absorption optical depths τ for 11.5-μm radiation for four scenes used in this study. These values were transformed from Landsat-inferred 0.83-μm optical depths by multiplying by 0.46. Table 1 lists some information about these images.

3. Data

Fields of optical depth inferred from 45 Landsat images of MBL clouds were employed [see Barker et al. (1996) for a summary]. Each image is 60 km^2, of which 41 consist of 2048^2 pixels while the others consist of 1024^2 pixels. They were presented originally by Harshvardhan et al. (1994), who used 0.83-μm nadir radiances to derive cloud extinction optical depths $\tau_{0.83}$ at horizontal resolution of either 28.5 or 57 m (Wielicki and Parker 1994). Thus, each image has its own $p(\tau|1)$. Use of these $p(\tau|1)$ for radiative flux calculations seems adequate for at least two reasons. First, at these resolutions, the vast majority of individual clouds are resolved very well (Wielicki and Welch 1986). Second, since the amplitude of variations in τ are known to decay rapidly for spatial scales less than ~500 m (e.g., Cahalan and Snider 1989), fluctuations at scales less than ~60 m are likely to be inconsequential for radiative transfer calculations.

Assuming the effective radius of cloud droplets r_e to be 10 μm (Han et al. 1994), extinction optical depth for wavelength 11.5 μm is approximately equal to $0.78\tau_{0.83}$, and ω_0 for 11.5-μm radiation is approximately 0.41 (Hu and Stamnes 1993). Hence, for this study, values of $\tau_{0.83}$ are transformed into absorption optical depths for 11.5-μm radiation as

$$\tau \approx (1 - 0.41)(0.78)\tau_{0.83} \approx 0.46\tau_{0.83}. \quad (7)$$

While results are presented for all 45 scenes, additional details are provided for the four scenes shown in Fig. 2: two examples each of broken stratocumulus and scattered cumulus. Table 1 lists information about these

TABLE 1. Summary of the four Landsat scenes shown in Fig. 2. Here A_c is vertically projected cloud fraction, $\bar{\tau}$ is mean 11.5-μm absorption optical depth for clouds only, and ν is the gamma function parameter obtained from Landsat-inferred values of τ: $\nu = (\bar{\tau}/\sigma)^2$, where σ is standard deviation of τ for clouds only. These quantities correspond to zenith radiances (i.e., $\mu = 1$).

Scene	Date (d/mo/yr)	Lat/Long	A_c	$\bar{\tau}$	ν
B2	10/7/87	31.17°N/129.45°W	0.644	1.58	1.251
B13	13/7/87	20.71°S/74.80°W	0.974	3.19	1.068
C7	8/7/90	33.18°N/33.81°W	0.256	3.98	0.669
C12	15/6/87	7.22°S/115.58°W	0.226	2.79	0.189

scenes. Detailed results are not presented for an overcast example because their distributions of τ are sufficiently narrow and $\bar{\tau}$ are sufficiently large (Barker et al. 1996) that LW transmittance and emissivity biases arising from the PPH assumptions are minor.

4. Monte Carlo experiments

This section presents results from a 3D Monte Carlo (MC) photon transport algorithm (Barker and Liu 1995) initialized with fields of Landsat-inferred τ (the 11.5-μm absorption optical depths). In the MC experiments, cyclic horizontal boundary conditions were assumed and since absorption optical depths were used, $\omega_0 = 0$. Cloudy pixels were modeled as vertically homogeneous columns with constant top elevation and variable geometric depth prescribed (in meters) as

$$h = 75.9\tau^{2/3}, \tag{8}$$

which is a good approximation to the Minnis et al. (1992) curve fit. While this prescription for cloud thickness is certainly not perfect, it is shown later that it yields reasonable standard deviations for h. All-sky MC transmittances T were computed by showering the arrays with isotropic distributions of ~3.7 million photons. From (3), T can be defined as

$$T = 1 - \hat{A}_c + 2\int_0^1 A_c(\mu)\mathcal{T}(\mu)\mu\, d\mu, \tag{9}$$

where $\mathcal{T}(\mu)$ is zenith-angle-dependent, mean *cloud* transmittance. Since τ was accumulated for each photon, $\hat{A}_c$ is defined as the fraction of photons that accumulated $\tau > 0$. To generate the μ-dependent functions, μ-specific simulations were performed at select angles for μ between 0.2 and 1.0.

First, consider the approximation of decoupling cloud fraction and cloud transmittance. This leads to (5) and was tested here by simply assessing how well

$$2\int_0^1 A_c(\mu)\mathcal{T}(\mu)\mu\, d\mu \approx \hat{A}_c\left[2\int_0^1 \mathcal{T}(\mu)\mu\, d\mu\right] \equiv \hat{A}_c T_{\text{cld}}^{\text{mc}}. \tag{10}$$

Figure 3 shows the left- and right-hand sides of (10) plotted against each other for all 45 scenes. Clearly, the error in this decoupling approximation is very small and leads to only a slight, but systematic, overestimation of the cloud contribution to overall transmittance (<0.01 at most).[1] That the largest differences tend to be associated with the smallest values of $A_c(1)$ (not shown) indicates further that, for all-sky transmittances, this approximation is adequate. This, therefore, is taken as justification to use (5).

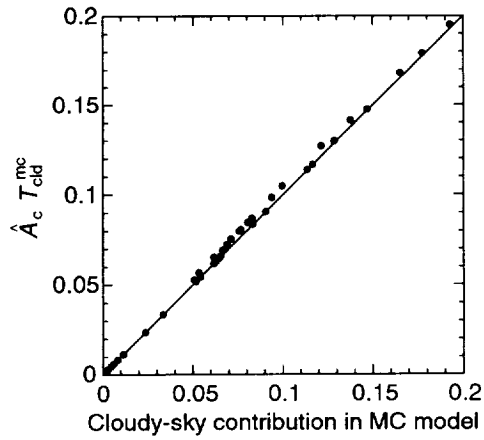

FIG. 3. Cloudy-sky contribution to overall transmittance as computed by the Monte Carlo algorithm (abscissa) plotted against the product of Monte Carlo determined hemispherical cloud fraction $\hat{A}_c$ and mean cloudy-sky transmittance $T_{\text{cld}}^{\text{mc}}$ (ordinate) for 45 Landsat scenes [see Eq.(10)]. Points on the diagonal line indicate near equality in (10).

The next two tests have a bearing on how well $p(\tau|\mu)$ can be approximated by simply $p(\tau|1)$. The fitted relations presented below were confined to $\mu \geq 0.2$: they tended to break down often for $\mu < 0.2$. This limitation poses little problem for flux quantities, however, as 96% of an isotropic beam is within $\mu \geq 0.2$.

Figure 4a shows $\bar{\tau}(\mu)$ for the four scenes in Fig. 2. The value of $\bar{\tau}(\mu)$ tends to decrease slightly as μ decreases on account of increased exposure of thin corners on the rectangular columns of cloud. In most cases, $\bar{\tau}(\mu)$ can be fit very well with the regression line

$$\bar{\tau}(\mu) \approx \bar{\tau}(1) + a_1(1 - \mu), \tag{11}$$

where a_1 is a coefficient determined by least-squares linear regression (as are all coefficients in this section). Figure 4b shows that for the most part, $a_1 \approx 0$ can be expected. Moreover, scenes that comply worst with (11) (i.e., smallest coefficients of determination R^2) are associated with very small, and irrelevant, values of a_1. The outlier with $A_c(1) \approx 0.53$ was observed at a solar zenith angle θ_0 of 69° (most others were at $\theta_0 \approx 30°$)

[1] If $A_c(\mu) = a\mu^b$, which is often an excellent fit (as shown later), and $\mathcal{T}(\mu) = \alpha + \beta\mu + \gamma\mu^2$, which is also a good representation, it is straightforward to show that $2\int_0^1 A_c(\mu)\mathcal{T}(\mu)\,\mu\, d\mu \leq \hat{A}_c T_{\text{cld}}^{\text{mc}}$ if $b \leq 0$, which is true for the clouds considered here.

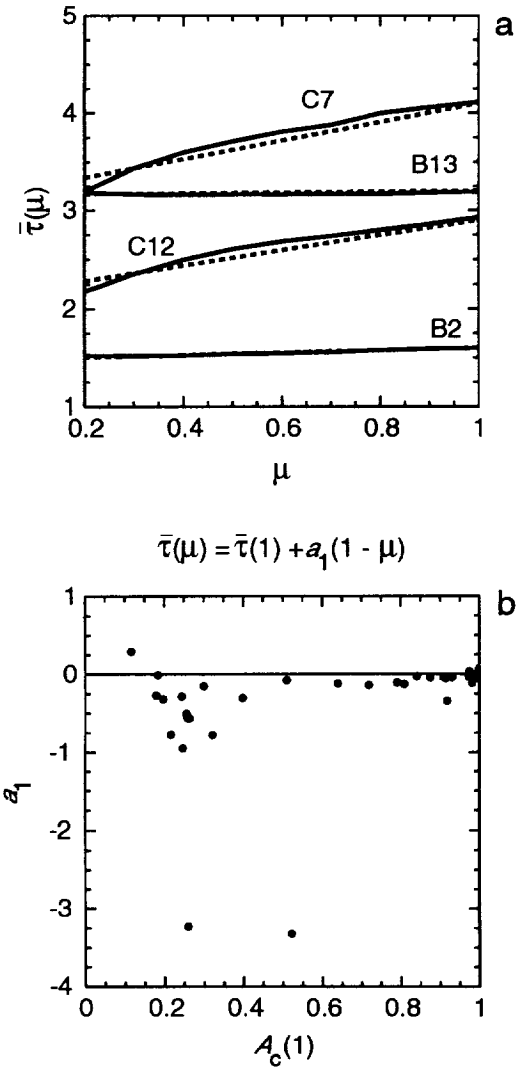

FIG. 4. (a) Solid lines are $\bar{\tau}(\mu)$ as determined by the Monte Carlo algorithm for the four scenes shown in Fig. 2. Broken lines are least-square linear regression fits of the form listed at the top of (b), [see also (11)]. (b) Slope coefficients a_1 for the fits of (11) to 45 scenes as a function of corresponding $A_c(1)$.

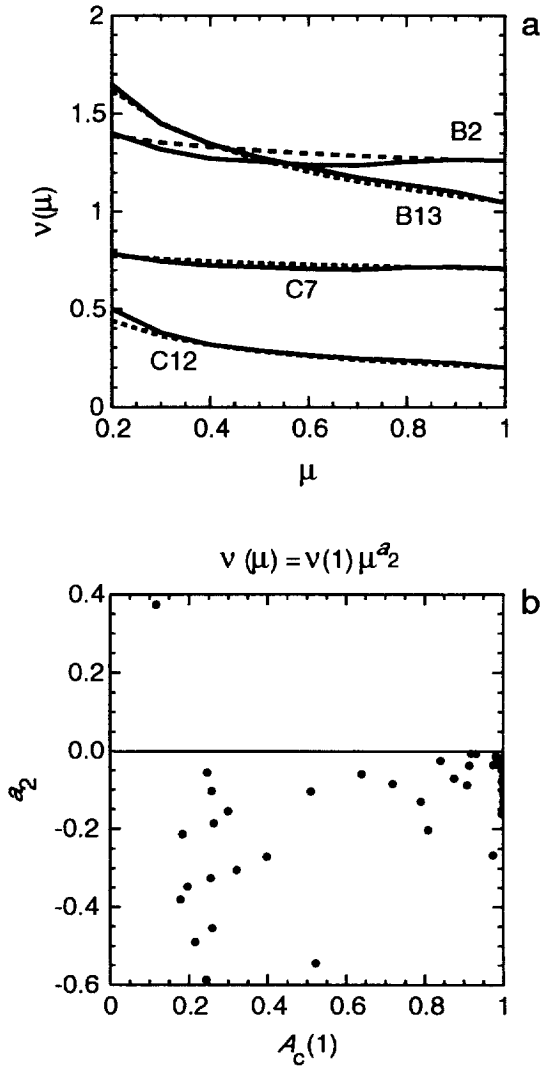

FIG. 5. (a) Solid lines are $\nu(\mu)$ as determined by the Monte Carlo algorithm for the four scenes shown in Fig. 2. Broken lines are least-square linear regression fits of the form listed at the top of (b) [see also (12)]. (b) Exponent coefficients a_2 for the fits of (12) to 45 scenes as a function of corresponding $A_c(1)$.

and this could be problematic (cf. Loeb and Coakley 1997). Roughly speaking, the quantity of concern for flux transmittances is similar to $\mu e^{-\bar{\tau}(\mu)/\mu}$ and so minor changes in $\bar{\tau}(\mu)$ with respect to μ are negligible because $\mu e^{-\bar{\tau}(\mu)/\mu}$ generally approaches zero rapidly as μ decreases.

Let the quantity $\nu(\mu) = [\bar{\tau}(\mu)/\sigma(\mu)]^2$, where $\sigma^2(\mu)$ is zenith-angle-dependent variance of τ, be a measure of relative magnitude of horizontal variability. Figure 5a shows that $\nu(\mu)$ tends to increase slightly with decreasing μ. Since $\bar{\tau}(\mu) \approx$ const, this means that $\sigma^2(\mu)$ decreases as μ decreases, which is not surprising and follows from the discussion in section 2 regarding smoothing via horizontal sampling by off-zenith radiances. The curves for $\nu(\mu)$ in Fig. 5a are described well by

$$\nu(\mu) \approx \nu(1)\mu^{a_2}, \tag{12}$$

where a_2 is again a regression coefficient. Figure 5b shows a_2 as a function of $A_c(1)$ for the 45 scenes. In general, the smaller $A_c(1)$, the more smoothing takes place for off-zenith trajectories. Again, (12) fits worst when a_2 is small, implying that (12) is an adequate model that tends to break down only when the trend it attempts to capture is of negligible importance. As in Fig. 4b, the outlier with $A_c(1) \approx 0.53$ is again an outlier in Fig. 5b. The value of a_2 for scenes B13 and C12 are relatively large at about -0.3, and from Fig. 5a it can be seen that this indicates that for most scenes and most

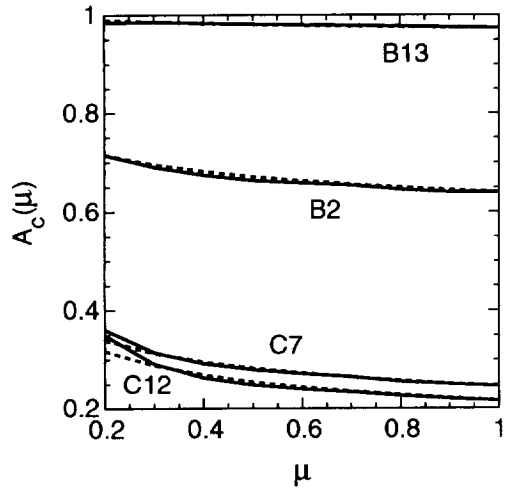

FIG. 6. Solid lines are $A_c(\mu)$ as determined by the Monte Carlo algorithm for the four scenes shown in Fig. 2. Broken lines are least square linear regression fits of the form shown in (13).

μ, $\nu(\mu) \approx \nu(1)$: only at small μ does $\sigma(\mu)$ become significantly small, but the contribution of the associated transmittances to the hemispherically integrated transmittance is quite small also. Hence, there appears to be very little reason to encumber a parameterization with $\nu(\mu)$. Furthermore, the μ dependence of $\bar{\tau}(\mu)$ and $\sigma^2(\mu)$ tend often to be in opposition: as μ decreases, reducing $\bar{\tau}(\mu)$ enhances transmittance, while enhancing $\nu(\mu)$ reduces it (cf. Barker et al. 1996).

For simplicity, μ dependencies of $\bar{\tau}(\mu)$ and $\nu(\mu)$ are neglected hereinafter and referred to as just $\bar{\tau}$ and ν, which are taken to be equivalent to $\bar{\tau}(1)$ and $\nu(1)$. Thus far, the results of this section indicate, fortunately, that simple parameterizations of $T_{\text{cld}}^{\text{mc}}$, such as by the conventional independent pixel approximation (IPA) (Cahalan et al. 1994a, b; Barker 1996), can be applied with confidence.

The next stage examines the necessity of having to use $\hat{A}_c$ as cpposed to, for example, simply $A_c(1)$, which may be the cloud fraction most people think of as predicted by GCMs and reported in cloud climatologies. Figure 6 shows values of $A_c(\mu)$ for the scenes shown in Fig. 2. It also shows that for most μ, $A_c(\mu)$ are approximated very well by

$$A_c(\mu) \approx A_c(1)\mu^{a_3}, \tag{13}$$

where a_3 is a regression coefficient that depends on distributions of cloud size, spacing, and aspect ratio. Note that the magnitude of a_3 for scene C12 is the largest of the four shown, and from Fig. 2 it can be seen that its clouds are small and spread quite uniformly over the field. Thus, it is easy to see why for decreasing μ, $A_c(\mu)$ increases so much relative to $A_c(1)$. Clouds in scenes B2 and C7, however, are more clustered and this results in smaller values of a_3 (clear lines-of-sight are difficult to close until very small μ). Figure 7a shows that for the 45 scenes, a_3 is correlated fairly well with vertically

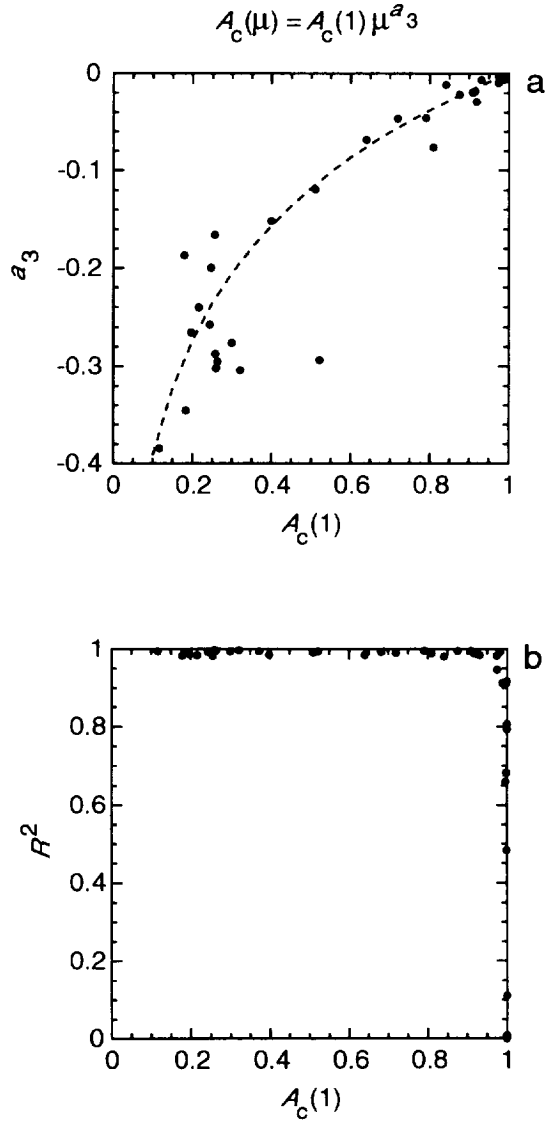

FIG. 7. (a) Exponent coefficients a_3 for the fits of (13) (see Fig. 6) to 45 scenes as a function of corresponding $A_c(1)$. Broken line is a least-square linear regression fit defined in (15). (b) Coefficients of determination R^2 for the fits listed at the top of the plot as a function of $A_c(1)$.

projected cloud fraction $A_c(1)$. For reasons just alluded to, the tendency in Fig. 7a is the smaller $A_c(1)$, the greater the dependence of $A_c(\mu)$ on μ. Figure 7b shows R^2 that result from fitting (13) for all 45 scenes as a function of $A_c(1)$. Most cases exhibit $R^2 > 0.98$, implying excellent fits. As with $\nu(\mu)$ and $\bar{\tau}(\mu)$, the few cases with poor fits are near overcast with very small, and irrelevant, values of a_3. Again, the scene with $A_c(1) \approx 0.53$ has an anomalously small value of a_3. Oddly, however, Fig. 7b shows that for this scene the fit in (13) is excellent.

Substitution of (13) into (4) leads to

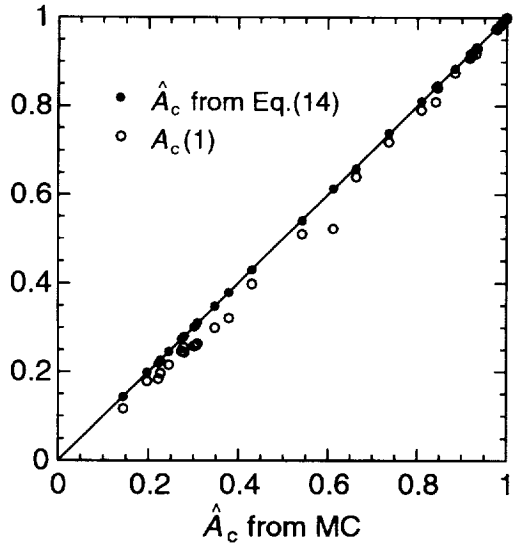

FIG. 8. Filled and empty circles are hemispherical cloud fractions $\hat{A}_c$ estimated by (14) and vertically projected cloud fractions $A_c(1)$, respectively, plotted as functions of corresponding $\hat{A}_c$ as determined directly from the Monte Carlo simulations for all 45 scenes.

$$\hat{A}_c \approx \frac{2A_c(1)}{a_3 + 2}, \tag{14}$$

which converges for $a_3 > -2$, though judging from Fig. 7a, it appears unlikely that a_3 will be < -0.5. Regardless of the fact that (13) yields $A_c(\mu) > 1$, the small values of a_3 limit this usually to very small μ. This has little impact on estimates of $\hat{A}_c$, as can be seen in Fig. 8, which compares $\hat{A}_c$ determined by (14) with that obtained directly from the MC simulations. The agreement is almost perfect as all points lie virtually atop the 1:1 line (despite a_3 being based on values for $\mu \geq 0.2$). When a_3 is parameterized by the regression line (see Fig. 7a)

$$a_3 \approx 0.17 \ln A_c(1) \tag{15}$$

and used in (14), estimates of $\hat{A}_c$ are almost as good as those shown in Fig. 8. Incidentally, use of (15) in (13) implies that, regardless of $A_c(1)$, $A_c(\mu) > 1$ only for $\mu \leq e^{-1/0.17} \approx 0.0028$. Figure 8 also shows that the largest difference between $\hat{A}_c$ and corresponding $A_c(1)$ is ~ 0.1 (or 20%), which is for the same scene responsible for the anomalous values in Figs. 4, 5, and 7 [see scene B11 in Barker et al.'s (1996) Fig. 1]. For the most part, however, relative differences between $\hat{A}_c$ and $A_c(1)$ are typically only about 5%. Since errors in cloud fraction affect both clear and cloudy components of (5a), it may be necessary, at times, to consider distinguishing between $\hat{A}_c$ and $A_c(1)$ in GCMs. As shown later, something as simple as (14) and (15) will likely suffice (see appendix A for an alternate approach).

The final part of this section compares the magnitudes of all-sky transmittance biases due to (i) neglect of cloud sides [i.e., use of $A_c(1)$ as opposed to $\hat{A}_c$], and (ii) neglect of horizontal variable τ (i.e., use of $T_{\text{cld}}^{\text{pp}}$ as opposed to $T_{\text{cld}}^{\text{mc}}$). This is achieved by examining the transmittances biases

cloud side bias:

$$\Delta T_{A_c} \equiv \{1 - A_c(1) + A_c(1) T_{\text{cld}}^{\text{mc}}\} - T$$

variable τ bias:

$$\Delta T_{\tau} \equiv \{1 - \hat{A}_c + \hat{A}_c T_{\text{cld}}^{\text{pp}}(\bar{\tau})\} - T, \tag{16}$$

where T is all-sky transmittance from the MC simulations and the terms in braces are approximate formulas. Hence, ΔT_{A_c} is informed of true Monte Carlo cloud transmittances but has no information about cloud sides. On the other hand, ΔT_{τ} has Monte Carlo information about cloud sides but no information about horizontal variability of τ. Figure 9 shows ΔT_{A_c} and ΔT_{τ} for all 45 scenes plotted against $A_c(1)$, $\bar{\tau}$, and ν. Clearly, the dominant bias is that due to variable τ as the magnitude of ΔT_{τ} is typically 2–5 times larger than ΔT_{A_c} for $A_c(1) \leq 0.9$. The largest values of ΔT_{τ} are between -0.1 and -0.15 and occur for scenes with $A_c(1)$ near 0.75 (these are roughly 30%–50% relative biases, given that T for these cases are ~ 0.4). The preference for ΔT_{τ} to be maximal for $\nu \approx 1$ is the result of a balance between having sufficiently many clouds to impact strongly the all-sky signal, but not too much cloud for, as $A_c(1) \to 1$, horizontal variability tends to weaken (Barker et al. 1996). Likewise, despite high variability (small ν) when $A_c(1)$ is very small (Barker et al. 1996), clouds contribute weakly to all-sky transmittance, thus reducing ΔT_{τ}. Relative biases for all-sky emissivity due to neglect of variable τ are between +10% and +30% for the majority of scenes.

Conversely, Fig. 9 shows that ΔT_{A_c} tends to be greatest for $A_c(1)$ near 0.3, which often have $\nu < 1$. When ν and $A_c(1)$ are small, and $\bar{\tau}$ is even just moderately large, there are sufficiently many deep clouds to initiate a large zenith angle dependence on cloud fraction (see Fig. 7a). Since this bears directly on the weighting of clear-sky transmittance, the cloud side bias is understandably largest for small cloud fractions. Of the 45 scenes, only scene B11 [see Barker et al.'s (1996) Fig. 1] has $|\Delta T_{A_c}| > |\Delta T_{\tau}|$ (again the scene responsible for the anomalous points in previous plots). Having been viewed at large θ_0, inferred values of $\tau_{0.83}$ can be anomalously large on the sunlit side of clouds (Barker and Liu 1995), and this would lead to excessive values of both h and a_3. Also, note that while ΔT_{A_c} decreases slowly with increasing $A_c(1)$, vanishing for overcast, ΔT_{τ} for near overcast conditions ranges from 0 to about -0.06.

Since ΔT_{A_c} and ΔT_{τ} are of opposite sign, neglect of both cloud sides and variable τ (as in conventional PPH models) will yield biases between those plotted in Fig. 9 but with a strong tendency to be negative (i.e., too little transmittance). Hence, it can be expected that GCMs under- and overestimate transmittances and emissivities, respectively, for MBL cloud fields. The main

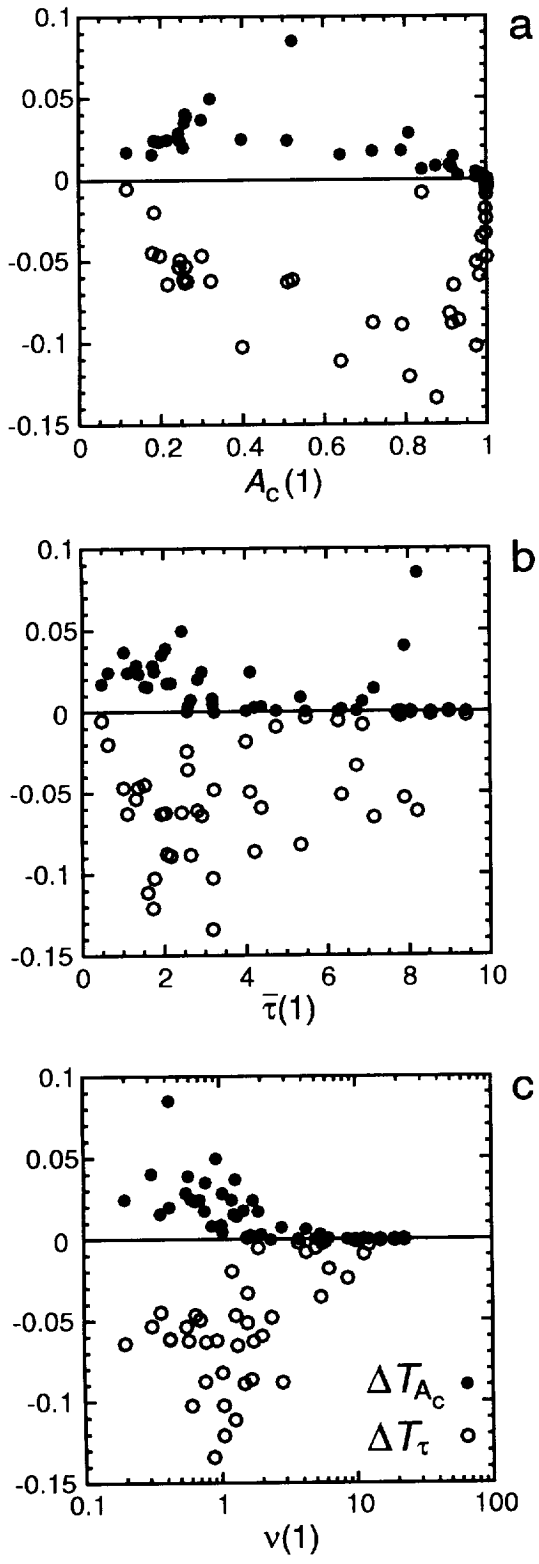

FIG. 9. Transmittance biases due to omission of (i) cloud side effects, ΔT_{A_c}; and (ii) horizontally variable τ, ΔT_τ, plotted as functions of corresponding (a) $A_c(1)$, (b) $\bar{\tau}$, and (c) ν for all 45 scenes. See text and (16) for details.

conclusion of this section, therefore, is that a simple parameterization for $\hat{A}_c$, like (14) and (15) for example, should suffice, while more attention should be paid to the impact of horizontally variable τ. This is addressed in the next section, which presents a simple parameterization for T_{cld}.

5. A parameterized model for T_{cld}

Having established that (5a) and $p(\tau|1)$, hereinafter referred to as simply $p(\tau)$, are likely to be adequate approximations for MBL clouds, this section presents a parameterization for T_{cld}, as defined in (5b), that may be useful for climate modeling studies. It is essentially an independent pixel approximation IPA based on the assumption that frequency distributions of τ often follow gamma distributions.

Barker et al. (1996) demonstrated that for MBL clouds, Landsat-inferred $p(\tau)$ are often represented very well by the normalized gamma distribution function, which can be written as

$$p_\Gamma(\tau) = \frac{1}{\Gamma(\nu)}\left(\frac{\nu}{\bar{\tau}}\right)^\nu \tau^{\nu-1} e^{-\nu\tau/\bar{\tau}}; \qquad \{\tau > 0;\ \nu > 0\}, \tag{17}$$

where $\Gamma(\nu)$ is the gamma function. Chambers et al. (1997) have demonstrated that Landsat-inferred $p(\tau)$, as used by Barker et al. (1996), are reliable. Moreover, $p(\tau)$ produced by cloud resolving models for MBL clouds are also described well by $p_\Gamma(\tau)$ (S. Krueger and B. Stevens, 1996, personal communication). Additionally, Barker (1996) derived an IPA for computing solar radiative fluxes for horizontally inhomogeneous MBL clouds based on $p_\Gamma(\tau)$. The parameter ν defines the form of $p_\Gamma(\tau)$, but lacks a unique definition. For example, Barker et al. (1996) used the method of moments, as above, to estimate ν as

$$\nu = (\bar{\tau}/\sigma)^2. \tag{18a}$$

Alternatively, the maximum likelihood estimate requires solving

$$\psi(\nu) + \ln\left(\frac{\bar{\tau}}{\nu}\right) - \overline{\ln\tau} = 0, \tag{18b}$$

where

$$\psi(\nu) = \frac{d}{d\nu}\ln\Gamma(\nu). \tag{18c}$$

While the value of ν depends on the method of solution, differences are generally less than 20%.[2]

[2] Exponentiating and rearranging (18b) leads to $e^{\overline{\ln\tau}}/\bar{\tau} = e^{\psi(\nu)}/\nu$, which also equals the τ reduction factor in Cahalan et al.'s (1994a) effective thickness approximation.

Substituting (17) into (5b), it can be shown (see appendix B) that

$$T^{\Gamma}_{\text{cld}} = x^{\nu}\left\{1-(1-x)\left[\nu-(\nu+1)\overline{\tau}\sum_{n=0}^{\infty}\frac{x^{n+1}}{\nu+2+n}\right]\right\}$$
$$= 1-\varepsilon^{\Gamma}_{\text{cld}}, \qquad (19)$$

where

$$x = \frac{\nu}{\nu+\overline{\tau}},$$

and the superscript Γ indicates that (17) has been used. Note that the leading term on the right of (19) is transmittance for normal incident radiance and approaches $e^{-\overline{\tau}}$ as $\nu \to \infty$. Also, as $\overline{\tau} \to \infty$, $T^{\Gamma}_{\text{cld}} \sim \overline{\tau}^{-\nu}$, whereas $T^{\text{PP}}_{\text{cld}} \sim e^{-\overline{\tau}}/\overline{\tau}$. For typical values of $\overline{\tau}$ and ν, the series in (19) converges to 10^{-4} in less than 10 terms and often in less than five terms. This confines errors in T^{Γ}_{cld} to the fifth decimal place, thus making accurate determination of (19) efficient. As listed in appendix C, computational requirements of T^{Γ}_{cld} are often 1–5 times those of conventional methods of computing $T^{\text{PP}}_{\text{cld}}$. The only time (19) is overly cumbersome is when $\overline{\tau}$ is small and ν is large: these conditions, however, appear to be rare (Barker et al. 1996). Moreover, when ν is large it is adequate to revert to $T^{\text{PP}}_{\text{cld}}$. When ν is an integer, the infinite sum in (19) can be replaced by the finite sum (see appendix B)

$$\sum_{n=0}^{\infty}\frac{x^{n+1}}{\nu+2+n} = -\frac{1}{x^{\nu+1}}\left[\ln(1-x)+\sum_{n=1}^{\nu+1}\frac{x^n}{n}\right], \qquad (20)$$

which reduces greatly the time required to compute T^{Γ}_{cld} (see appendix C). This identity could be used globally if one is willing to round off ν to the nearest integer. This is not necessarily as harsh as it sounds given the magnitude of other uncertainties in GCM cloud properties. Rounding $\nu < 1$ to $\nu = 1$ would be undesirable given that $\partial T^{\Gamma}_{\text{cld}}/\partial\nu$ changes rapidly for $\nu < 1$. Moreover, Table C1 shows that for $\nu < 1$, (19) is efficient. Therefore, the rounding need only be done for $\nu > 1$, where $\partial T^{\Gamma}_{\text{cld}}/\partial\nu$ is relatively small. On the other hand, in an operational setting it may be desirable to use a 3D look-up table for (19).

Figure 10 shows that $T^{\text{PP}}_{\text{cld}}$ underestimates $T^{\text{mc}}_{\text{cld}}$ ($=2\int_0^1 \mathcal{T}(\mu)\mu\, d\mu$) by about an order of magnitude for $T^{\text{mc}}_{\text{cld}} \lesssim 0.2$ and 20%–100% otherwise. In fact, the overall values of mean bias error (MBE) and root-mean-square error (rmse) are −0.100 and 0.131, respectively. Conversely, overall values of MBE and rmse for T^{Γ}_{cld} relative to $T^{\text{mc}}_{\text{cld}}$ are +0.023 and 0.057, respectively. Thus, use of T^{Γ}_{cld} reduces the bias error by a factor of ~4 and the random error by a factor of ~2. Note that the positive bias for T^{Γ}_{cld} increases as $T^{\text{mc}}_{\text{cld}}$ increases [i.e., as ν and $\overline{\tau}$ tend to decrease; see Fig. 9 and Barker et al. (1996)]. This is due, in part, to the fact that T^{Γ}_{cld} is based on $\tau \in (0, \infty)$, while $T^{\text{mc}}_{\text{cld}}$ is based on Landsat-inferred τ, which has a minimum optical depth $\tau_{\min} > 0$. Thus, when ν is small (<1), a significant contribution to T^{Γ}_{cld} can come from $0 < \tau < \tau_{\min}$. Wielicki and Parker (1992) estimate that the fractional amount of optically thin MBL cloud ($\tau \lesssim 0.1$) undetected by Landsat visible reflectance thresholds is typically less than 0.05. Since transmittances for $\tau < \tau_{\min}$ are almost 1.0, the parameterized model interprets this as almost cloudless sky and so overestimates $T^{\text{mc}}_{\text{cld}}$. Therefore, to call this strictly an overestimation on the part of T^{Γ}_{cld} is not entirely true.

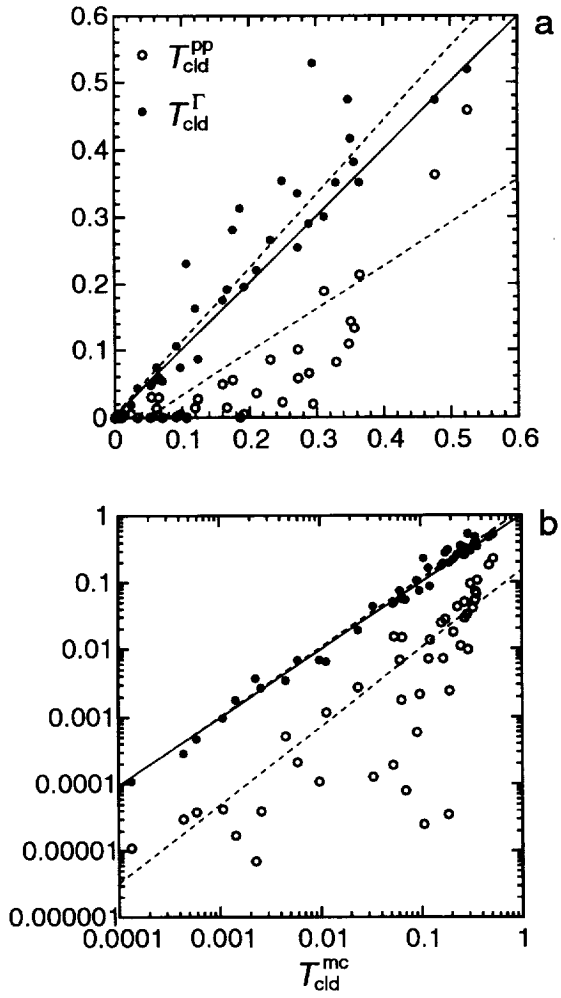

FIG. 10. Gamma-weighted transmittances T^{Γ}_{cld} computed by (19) using $\overline{\tau}$ and ν, and PPH transmittances $T^{\text{PP}}_{\text{cld}}$ computed using $\overline{\tau}$ for 45 Landsat scenes plotted as functions of Monte Carlo transmittances $T^{\text{mc}}_{\text{cld}}$. The only difference between the plots is the scale of their axes. Solid lines represent perfect model performance, while broken lines are regression fits to the points. In (a), regression lines are of the form $a + bT^{\text{mc}}_{\text{cld}}$ and are much determined by large transmittance cases. In (b), regression lines are of the form $a\,(T^{\text{mc}}_{\text{cld}})^b$ and are determined by small transmittance cases.

Figure 11 shows $\varepsilon^{\Gamma}_{\text{cld}}$ and $\varepsilon^{\text{PP}}_{\text{cld}}$, as defined in (19) and (6), plotted as functions of $\hat{A}_c$. Regardless of $\hat{A}_c$, $\varepsilon^{\text{PP}}_{\text{cld}}$ is almost always greater than 0.8. The stippled ellipse contains most of the Luo et al. (1994) estimates of daytime

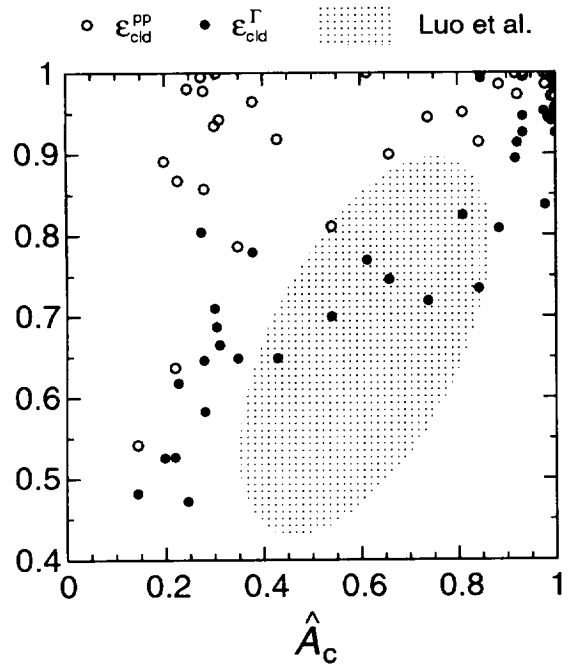

FIG. 11. Mean cloud emittances predicted by the gamma-weighted PPH $\varepsilon_{cld}^{\Gamma}$ and PPH ε_{cld}^{PP} models [see (19) and (6), respectively] as a function of hemispherical cloud fraction $\hat{A}_c$ for 45 Landsat scenes. The stippled ellipse encompasses most of Luo et al.'s (1994) estimates of 11-μm cloud emissivities for (250 km)^2 regions of ~1-km resolution AVHRR data viewed off the west coast of South America.

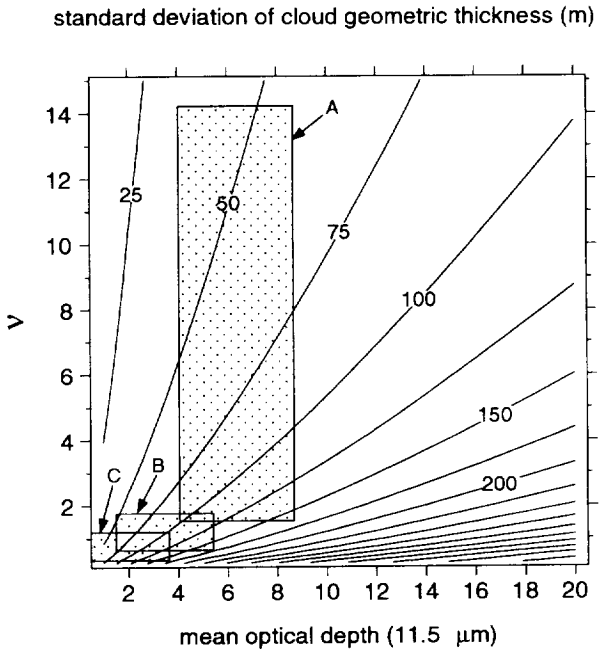

FIG. 12. Standard deviation of cloud geometric thickness h (in meters) as a function of $\bar{\tau}$ and ν. These were determined by considering h to be related to τ as in (8) and τ to be defined by the gamma distribution in (17). Stippled regions demarcate where most of the scenes lie that were used by Barker et al. (1996): (A) overcast; (B) broken stratocumulus; (C) scattered cumulus.

11-μm cloud emissivities for marine stratocumulus off the west coast of South America (see their Fig. 8). While their results are for (250 km)^2 images of ~1 km resolution Advanced Very High Resolution Radiometer data, they agree quite well with $\varepsilon_{cld}^{\Gamma}$. Values of $\varepsilon_{cld}^{\Gamma}$ for $\hat{A}_c \lesssim 0.4$ may, in reality, be shifted slightly down and right (i.e., closer to Luo et al.'s ellipse, which is not subject to the same shift as they used 11-μm radiances). This is because scenes with small cloud fractions (and small ν) tend to have many small values of τ and very thin clouds were certainly missed by Landsat (horizontal shift of probably <0.05) and as a result, $\bar{\tau}$ and ν (and thus mean emittance) were overestimated slightly (vertical shift down).

Finally, reconsider the prescription of cloud thickness h that was used to create 3D cloud fields [Eq. (8)]. Substituting (8) into (17) yields standard deviations of h, as shown in Fig. 12. Also shown are regions that contain the majority of scenes in three classes: (A) overcast stratocumulus, (B) broken stratocumulus, and (C) scattered cumulus (see Table 3 in Barker et al. 1996). For the most part, standard deviations of h are between 50 m and 125 m, which is in agreement with some observations (Loeb et al. 1997, manuscript submitted to *J. Atmos. Sci.*) and also fits well with a theoretical model (Considine et al. 1997).

6. Summary and conclusions

This paper presented a simple conceptual model for flux transmittance of longwave (LW) radiation through an inhomogeneous, marine boundary layer (MBL) cloud field. Two general aspects of cloud geometry were addressed: horizontal variability of optical depth τ and cloud sides. Using a 3D Monte Carlo photon transport algorithm and fields of τ inferred from 45 Landsat images, it was demonstrated that when cloud fraction is $\lesssim$0.9, neglect of horizontal variable τ leads to all-sky transmittance biases that are roughly 2–5 times larger than, and opposite in sign to, biases stemming from neglect of cloud sides.[3] As such, priority (in both research effort and computation) should be given to parameterizations that account for the impact of variable τ.

Regarding horizontal variability of τ, an approximate method for computing LW flux transmittances was furnished. It is essentially a stochastic radiative transfer model whose validity rests on the assumption that frequency distributions of optical depth $p(\tau)$, for (60 km)^2 regions, are often approximated well by gamma distri-

[3] This disparity in biases may be much ameliorated, or even reversed, for land cumulus, which exhibit both sharper edges (Wielicki and Parker 1992) and greater vertical extent than MBL clouds. This is the subject of a later study.

bution functions (Barker et al. 1996). This method is computationally efficient and suitable for GCMs. It was also demonstrated that the standard plane-parallel, homogeneous (PPH) model often underestimates cloud transmittances by about an order of magnitude for thick clouds and by 20%–100% for thinner clouds. Conversely, when the mean and standard deviation of τ are used to define a gamma distribution, the gamma-weighted PPH removes typically more than 80% of the homogeneous bias. While this model neglected scattering, inclusion of it should not alter results much (a similar model with scattering is under development).

It was shown that, in principle, cloud fraction and radiation cannot be decoupled. But, for computation of fluxes for MBL clouds, the conventional technique of weighting clear- and cloudy-sky transmittances by suitable clear- and cloudy-sky fractions is acceptable (cf. Stephens 1988). But what is a suitable cloud fraction? Real clouds have depth and therefore, vertically projected cloud fractions A_c differ from cloud fractions $\hat{A}_c$ presented to an isotropic beam of radiation. It is not obvious what cloud fractions GCM modelers think their radiation models are, and should, be using. Here $\hat{A}_c$ is the more relevant quantity for computing fluxes, but it can be expected to be a complex function of cloud aspect ratios and spatial arrangement of clouds. Despite this, a simple parameterization of $\hat{A}_c$ as a function of A_c was offered based on the 45 MBL cloud fields used here.

Thus, the main recommendation stemming from this study is: the LW radiative effects of horizontal variable τ for MBL clouds should be included in GCM radiation routines in conjunction with due consideration of the effects of enhanced cloud fraction arising from hemispherical integration of cloud side view-factors. Since the combined effect of horizontal variability of τ and cloud sides is to reduce cloud emittance relative to PPH conditions, the immediate impact of using the parameterizations presented here in a GCM would be a slight warming of MBL clouds (which would not be undesirable for many GCMs). As a final note, while the magnitude of LW biases presented here are comparable to their solar counterparts (Cahalan et al. 1994a; Barker et al. 1996), LW biases may dominate at times as they act continuously.

Acknowledgments. The authors wish to thank Lindsay Parker (Lockheed-Martin Engineering and Science Company) for processing of Landsat data and Lazaros Oreopoulos and Ismail Gultepe (AES-Downsview) for helpful comments.

APPENDIX A

An Alternate Approach to Estimate $\hat{A}_c$

A somewhat more attractive technique for describing $A_c(\mu)$, which fits the MC results about as well as (13), is

$$A_c(\mu) \approx 1 - [1 - A_c(1)]e^{-a_4 \tan\theta} = 1 - [1 - A_c(1)] \exp\left[-a_4 \frac{\sqrt{1-\mu^2}}{\mu}\right], \quad \text{(A1)}$$

where a_4 is a coefficient and θ is zenith angle. This corresponds to identical cylinders distributed on a plane according to Poisson's law (Avaste et al. 1974) and has been used to describe $A_c(\mu)$ by Ellingson (1982) and Barker et al. (1993), while Otterman (1984) used it in his vegetation albedo model to describe direct-beam interception. The reason this might be considered more attractive than (13) is because it confines $A_c(\mu) \in [0, 1]$. Substituting (A1) into (4) yields

$$\hat{A}_c \approx A_c(1) + [1 - A_c(1)] \times a_4[\mathrm{Ci}(a_4)\sin(a_4) - \mathrm{si}(a_4)\cos(a_4)] = A_c(1) + [1 - A_c(1)]f(a_4), \quad \text{(A2)}$$

where Ci is the cosine integral and si = Si $-\pi/2$ in which Si is the sine integral (Abramowitz and Stegun 1964). For the 45 Landsat scenes, a_4 was fitted with

$$a_4 \approx 0.03 + 0.07A_c(1), \quad \text{(A3)}$$

and $f(a_4)$ was parameterized by

$$f(a_4) \approx \frac{-29.194a_4}{-20.248 - a_4(27.729 + a_4)}, \qquad a_4 \in [0, 1], \quad \text{(A4)}$$

which has a maximum error of 0.0025. Hence, (A2) through (A4) is almost as efficient as (14) and (15).

The reason why (13) through (15) was used in this study rather than this technique was simply because it performed slightly better. This is not to say that the method presented in this appendix performed poorly; it just had a minor tendency to overestimate Monte Carlo values of $\hat{A}_c$. Nonetheless, it was presented here anyway as future studies (such as with land cumulus, perhaps) might find this approach more appropriate.

APPENDIX B

Derivation of Eqs. (19) and (20)

Substituting (17) into (5b) and carrying out the integration with respect to μ first yields

$$T^{\Gamma}_{\mathrm{cld}} = \frac{2}{\Gamma(\nu)}\left(\frac{\nu}{\bar{\tau}}\right)^{\nu} \int_0^{\infty} E_3(\tau)\tau^{\nu-1}e^{-\nu\tau/\bar{\tau}}\, d\tau. \quad \text{(B1)}$$

Substituting

$$E_3(\tau) = \frac{1}{2}\{e^{-\tau} - \tau e^{-\tau} + \tau^2 E_1(\tau)\} \quad \text{(B2)}$$

into (B1) gives

$$T^{\Gamma}_{cld} = \frac{1}{\Gamma(\nu)}\left(\frac{\nu}{\bar{\tau}}\right)^{\nu}\left\{\left(\frac{\bar{\tau}}{\nu+\bar{\tau}}\right)^{\nu}\left[\Gamma(\nu) - \frac{\bar{\tau}}{\nu+\bar{\tau}}\Gamma(\nu+1)\right] + \int_0^{\tau} E_1(\tau)\tau^{\nu+1}e^{-\nu\tau/\bar{\tau}}\,d\tau\right\}. \quad \text{(B3)}$$

From Gradshteyn and Ryzhik (1980),

$$\int_0^{\tau} E_1(\tau)\tau^{\nu+1}e^{-\nu\tau/\bar{\tau}}\,d\tau = \left(\frac{\bar{\tau}}{\nu+\bar{\tau}}\right)^{\nu+2}\frac{\Gamma(\nu+2)}{\nu+2} \times {}_2F_1\left(1, \nu+2, \nu+3; \frac{\nu}{\nu+\bar{\tau}}\right), \quad \text{(B4)}$$

where ${}_2F_1(a, b, c; x)$ is the hypergeometric function. Since $1 + (\nu + 2) - (\nu + 3) = 0$ in (B4), ${}_2F_1$ in (B4) converges for all $\bar{\tau} > 0$ and $\nu > 0$ (Arfken 1970). Also for ${}_2F_1$ in (B4)

$${}_2F_1\left(1, \nu+2, \nu+3; \frac{\nu}{\nu+\bar{\tau}}\right) = (\nu+2)\sum_{n=0}^{\infty}\frac{1}{\nu+2+n}\left(\frac{\nu}{\nu+\bar{\tau}}\right)^{n}. \quad \text{(B5)}$$

Substituting (B5) into (B4), and (B4) into (B3), and rearranging yields (19) in the text.

When ν is an integer, the infinite sum in (19) can be replaced by the finite sum in (20) for which a proof is given here. Let the sum in (19) be represented by

$$S = \sum_{n=0}^{\infty}\frac{x^{n+1}}{n+(\nu+2)} = \sum_{m=1}^{\infty}\frac{x^{m}}{m+(\nu+1)}. \quad \text{(B6)}$$

Multiplying both sides of (B6) by $x^{\nu+1}$ gives

$$x^{\nu+1}S = \sum_{m=1}^{\infty}\frac{x^{m+(\nu+1)}}{m+(\nu+1)} = \sum_{k=\nu+2}^{\infty}\frac{x^{k}}{k}, \quad \text{(B7)}$$

which can also be written as

$$x^{\nu+1}S = \sum_{k=1}^{\infty}\frac{x^{k}}{k} - \sum_{k=1}^{\nu+1}\frac{x^{k}}{k}. \quad \text{(B8)}$$

Since

$$\sum_{k=1}^{\infty}\frac{x^{k}}{k} = -\ln(1-x), \quad \text{(B9)}$$

(B8) can be rewritten as

$$S = \frac{1}{x^{\nu+1}}\left[\ln(1-x) + \sum_{k=1}^{\nu+1}\frac{x^{k}}{k}\right], \quad \text{(B10)}$$

which is equivalent to (20) and completes the proof.

TABLE C1. CPU time required by an HP 725/75 workstation to compute T^{pp}_{cld} via both (C1) and (C2) normalized to the time required to compute (C2). Times for T^{Γ}_{cld} are also normalized to those required for (C2). For T^{Γ}_{cld}, values not in parentheses are for (19), while those in parentheses are for (20). For both T^{pp}_{cld} [using Eq. (C1)] and T^{Γ}_{cld} [using Eq. (19)], summations were terminated when the magnitude of the terms became less than 0.0001.

	T^{pp}_{cld} [using (C1)]	T^{pp}_{cld} [using (C2)]	T^{Γ}_{cld}		
$\bar{\tau}$			$\nu = 0.1$	$\nu = 1.0$	$\nu = 5.0$
0.46	1.30	1.0	1.18	3.76 (1.29)	11.09 (1.75)
2.3	0.66	1.0	1.18	1.87 (1.29)	4.06 (1.75)
6.9	0.66	1.0	1.18	1.52 (1.29)	2.47 (1.75)

APPENDIX C

Computational Considerations for T^{Γ}_{cld} and T^{pp}_{cld}

This appendix documents some computational considerations of the homogeneous solution T^{pp}_{cld} which utilizes $E_3(\tau)$, and the gamma-weighted solution T^{Γ}_{cld} as defined in (19). Here $E_3(\tau)$ is evaluated using

$$E_3(\tau) = \begin{cases} \dfrac{0.250621 + 2.334733\tau + \tau^2}{(1.681534 + 3.330657\tau + \tau^2)\tau e^{-\tau}}, & \text{for } \tau \geq 1 \\ \dfrac{\tau^2}{2}\left(\dfrac{3}{2} - \gamma - \ln\tau\right) - \sum\limits_{\substack{m=0 \\ m\neq 2}}^{\infty}\dfrac{(-\tau)^m}{(m-2)m!}, & \text{for } \tau < 1, \end{cases} \quad \text{(C1)}$$

as given by (Abramowitz and Stegun 1964), and also by the parameterization

$$E_3(\tau) = \exp\left[\frac{\sum_{n=1}^{5} a_n\tau^n}{\sum_{n=1}^{6} b_n\tau^n}\right], \quad \text{for } \tau \in [0, 100], \quad \text{(C2)}$$

which has maximum errors of 0.2% and 1.37% for $\tau < 55$ and $\tau < 100$, respectively, and

$a_1 = 2277326.0$ $b_1 = -3285487.0$

$a_2 = 18451521.0$ $b_2 = -17343648.0$

$a_3 = 36528961.0$ $b_3 = -11795192.0$

$a_4 = 15688104.0$ $b_4 = -1086098.3$

$a_5 = 1115332.6$ $b_5 = -253.0$

$b_6 = 1.0.$

Table C1 lists some CPU requirements for computation of T^{pp}_{cld} and T^{Γ}_{cld}.

REFERENCES

Abramowitz, M., and I. A. Stegun, 1964: *Handbook of Mathematical Functions*. Applied Mathematicals Series, Vol. 55, Washington Bureau of Standards. (Reprinted, Dover, 1968)

Arfken, G., 1970: *Mathematical Methods for Physicists.* Academic Press, 815 pp.

Avaste, O. A., Y. R. Mullamaa, K. Y. Niylisk, and M. A. Sulev, 1974: On the coverage of the sky by clouds. *Heat Transfer in the Atmosphere,* Ye. M. Feygel'son and L. R. Tsvang, Eds., NASA Tech. Trans. NASA TT-F-790, 173–181.

Barker, H. W., 1992: Solar radiative transfer for clouds possessing isotropic variable extinction coefficient. *Quart. J. Roy. Meteor. Soc.,* **118,** 1145–1162.

——, 1996: A parameterization for computing grid-averaged solar fluxes for inhomogeneous marine boundary layer clouds. Part I: Methodology and homogeneous biases. *J. Atmos. Sci.,* **53,** 2289–2303.

——, and D. Liu, 1995: Inferring optical depth of broken clouds from Landsat data. *J. Climate,* **8,** 2620–2630.

——, S. R. Pal, and A. I. Carswell, 1993: Infrared flux transmittances for inhomogeneous cirrus clouds. *IAMAP Int. Radiation Symp. 1992,* S. Keevallik and O. Karner, Eds., Deepak, 145–149.

——, B. A. Wielicki, and L. Parker, 1996: A parameterization for computing grid-averaged solar fluxes for inhomogeneous marine boundary layer clouds. Part II: Validation using satellite data. *J. Atmos. Sci.,* **53,** 2304–2316.

Cahalan, R. F., 1991: Landsat analysis of fractal cloud structure. *Non-Linear Variability in Geophysics,* D. Schertzer and S. Lovejoy, Eds., Kluwer, 281–295.

——, and J. B. Snider 1989: Marine stratocumulus structure. *Remote Sens. Environ.,* **28,** 95–107.

——, W. Ridgway, W. J. Wiscombe, T. L. Bell, and J. B. Snider, 1994a: The albedo of fractal stratocumulus clouds. *J. Atmos. Sci.,* **51,** 2434–2455.

——, ——, ——, S. Golmer, and Harshvardhan, 1994b: Independent pixel and Monte Carlo estimates of stratocumulus albedo. *J. Atmos. Sci.,* **51,** 3776–3790.

Chambers, L. H., B. A. Wielicki, and K. F. Evans, 1997: Accuracy of the independent pixel approximation for satellite estimates of oceanic boundary layer cloud optical depth. *J. Geophys. Res.,* **102,** 1779–1794.

Charlock, T., and B. M. Herman, 1976: Discussion of the Elsasser formulation for infrared fluxes. *J. Appl. Meteor.,* **15,** 657–661.

Coakley, J. A., Jr., and F. P Bretherton, 1982: Cloud cover from high resolution scanner data: Detecting and allowing for partially filled fields of view. *J. Geophys. Res.,* **87,** 4917–4932.

Considine, G. D., J. A. Curry, and B. A. Wielicki, 1997: Modeling cloud fraction and horizontal variability in marine boundary layer clouds. *J. Geophys. Res.,* **102,** 13 517–13 525.

Davis, A., P. Gabriel, S. Lovejoy, D. Schertzer, and G. Austin, 1990: Discrete angle radiative transfer—Part III: Numerical results and applications. *J. Geophys. Res.,* **95,** 11 729–11 742.

Ellingson, R. G., 1982: On the effects of cumulus dimensions on longwave irradiance and heating rate calculations. *J. Atmos. Sci.,* **39,** 886–896.

Elsasser, W. M., 1942: *Heat Transfer by Infrared Radiation in the Atmosphere.* Harvard Meteor. Studies, No. 6, Harvard University Press, 107 pp.

Evans, K. F., 1993: Two-dimensional radiative transfer in cloudy atmospheres: The spherical harmonic spatial grid method. *J. Atmos. Sci.,* **50,** 3111–3124.

Gradshteyn, I. S., and I. M. Ryzhik, 1980: *Table of Integrals, Series, and Products: Corrected and Enlarged Edition.* Academic Press, 1160 pp.

Han, Q., W. B. Rossow, and A. A. Lacis, 1994: Near-global survey of effective radii in liquid water clouds using ISCCP data. *J. Climate,* **7,** 465–497.

Harshvardhan, J. A. Weinman, and R. Davies, 1981: Transport of infrared radiation in cuboidal clouds. *J. Atmos. Sci.,* **38,** 2500–2513.

——, B. A. Wielicki, and K. M. Ginger, 1994: The interpretation of remotely sensed cloud properties from a model parameterization perspective. *J. Climate,* **7,** 1987–1998.

Hu, Y. X., and K. Stamnes, 1993: An accurate parameterization of the radiative properties of water clouds suitable for use in climate models. *J. Climate,* **6,** 728–742.

Loeb, N. G., and J. A. Coakley Jr., 1997: Inference of marine stratus cloud optical depths from satellite measurements: Does 1D theory apply? *J. Climate,* in press.

Luo, G., X. Lin, and J. A. Coakley Jr., 1994: 11 μm emissivities and droplet radii for marine stratocumulus. *J. Geophys. Res.,* **99,** 3685–3698.

Minnis, P., P. W. Heck, D. F. Young, C. W. Fairall, and J. B. Snider, 1992: Stratocumulus cloud properties derived from simultaneous satellite and island-based instrumentation during FIRE. *J. Appl. Meteor.,* **31,** 317–339.

Otterman, J., 1984: Albedo of a forest modeled as a plane with dense protrusions. *J. Climate Appl. Meteor.,* **23,** 297–307.

Plank, V. G., 1969: The size distribution of cumulus clouds in representative Florida populations. *J. Appl. Meteor.,* **8,** 46–67.

Quanhau, L., and J. Schmetz, 1987: On the problem of an analytic solution to the diffusivity factor. *Beitr. Phys. Atmos.,* **61,** 23–29.

Rossow, W. B., and R. A. Schiffer, 1991: ISCCP cloud products. *Bull. Amer. Meteor. Soc.,* **72,** 2–20.

Schertzer, D., and S. Lovejoy, 1987: Physical modelling and analysis of rain and clouds by anisotropic scaling multiplicative processes. *J. Geophys. Res.,* **92,** 9693–9714.

Stephens, G. L., 1978: Radiation profiles in extended water clouds. II: Parameterization schemes. *J. Atmos. Sci.,* **35,** 2123–2332.

——, 1988: Radiative transfer through arbitrarily shaped optical media. Part II: Group theory and simple closures. *J. Atmos. Sci.,* **45,** 1837–1848.

Welch, R. M., and B. A. Wielicki, 1984: Stratocumulus cloud field reflected fluxes: The effect of cloud shape. *J. Atmos. Sci.,* **41,** 3085–3103.

Wielicki, B. A., and R. M. Welch, 1986: Cumulus cloud properties using Landsat satellite data. *J. Climate Appl. Meteor.,* **25,** 261–276.

——, and L. Parker, 1992: The determination of cloud cover from satellite sensors: The effect of sensor spatial resolution. *J. Geophys. Res.,* **97,** 12 799–12 823.

——, and ——, 1994: Frequency distributions of cloud liquid water path in oceanic boundary layer cloud as a function of regional cloud fraction. Preprints, *Eighth Conf. on Atmospheric Radiation,* Nashville, TN, Amer. Meteor. Soc., 415–417.

Wylie, D. P., W. P. Menzel, H. W. Woolf, and K. L. Strabala, 1994: Four years of global cirrus cloud Statistics using HIRS. *J. Climate,* **7,** 1972–1986.

Zuev, V. E., and G. A. Titov, 1995: Radiative transfer in cloud fields with random geometry. *J. Atmos. Sci,* **52,** 176–190.